Chapter 4

Raw data processing

4.1 Data processing flow

The flow of the offline data processing is shown in Fig.4.1 The data transferred from the VAX are temporarily copied on the disk buffer of the FACOM M-1800. These data are recorded on magnetic cassette tapes (CTL). The capacity of the CTL is $\sim$ 280 MB. The data are converted to the TOPAZ standard data format to match our data handling system called TRISTAN Bank System (TBS). The formatted data are stored as raw data.

The contents of the raw data are direct electric output of such as Analogue-to-Digital Converter (ADC) and Time-to-Digital Converter (TDC). For physics analyses, it is necessary to convert them to physical quantities. They are reconstructed from the raw data in the following two steps, "reduction" and "production".

In the reduction step, the size of the data is reduced by rejecting obviously non-physics events such as beam-gas events. The events which satisfy none of the following conditions are rejected:

1. Total sum of BCL energy $>$ 4 GeV .AND. 360 nsec $< t <$ 390 nsec;
2. Partial sum of BCL energy $>$ 1 GeV .AND. 360 nsec $< t <$ 390 nsec;
3. Total sum of ECL energy $>$ 8 GeV .AND. 300 nsec $< t <$ 700 nsec;
4. Partial sum of ECL energy $>$ 2 GeV .AND. 300 nsec $< t <$ 700 nsec;
5. Existence of TPC trigger .AND. the number of TPC tracks with $\mid z \mid <$ 10 cm $\geq$ 1.

Where total sum and partial sum are defined in Section 3.3.1, t is the trigger timing measured form beam crossing, and $\mid z \mid$ is the absolute z coordinate of the

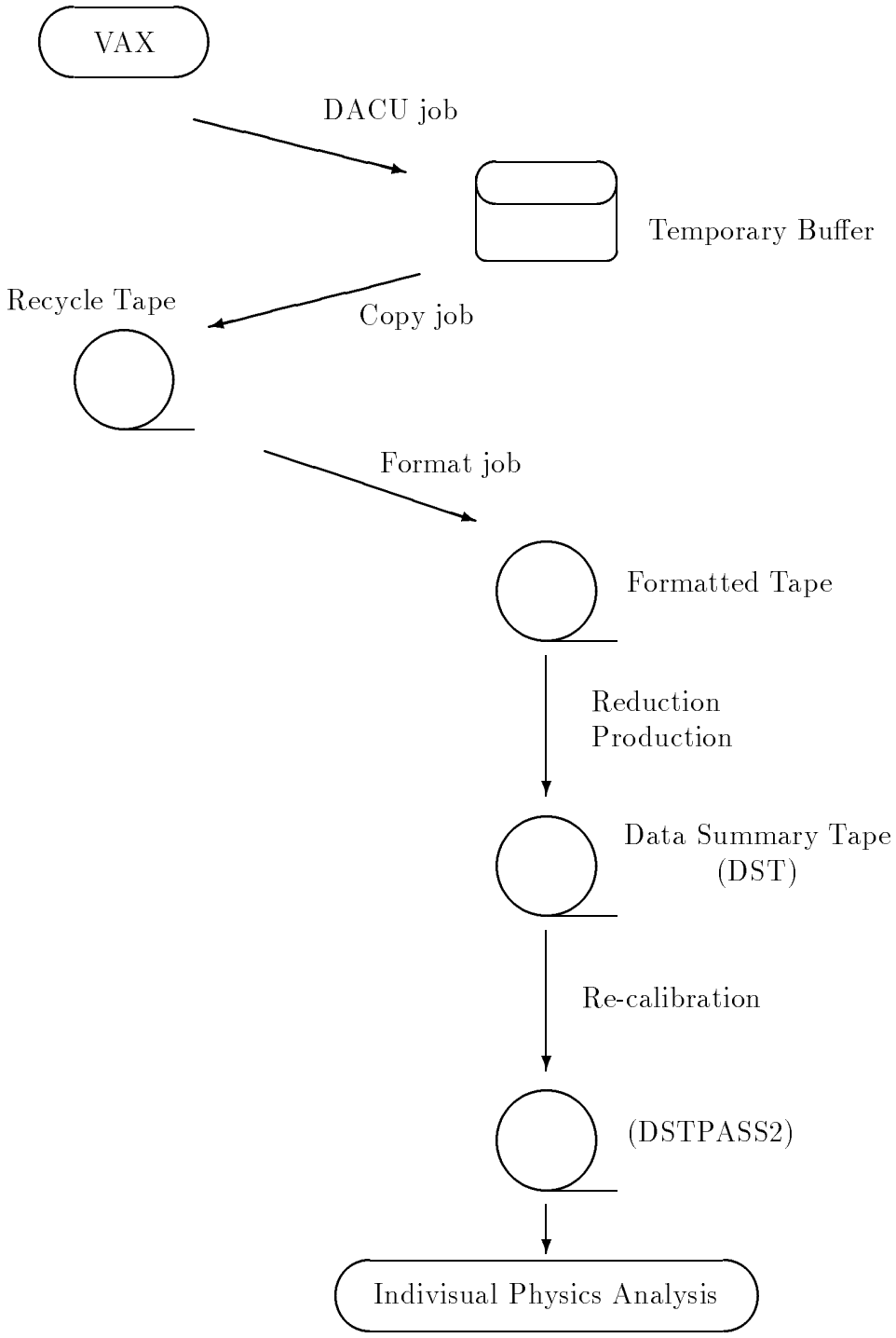

Figure 4.1: The flow diagram of the TOPAZ offline analysis.

track's closest approach to the z axis. By this condition, about 50% events are removed.

In the production step, the data which passed the reduction filters is converted to the following physical observables:

- the vertex position and momentum for each charged track,
- particle species for each charged track, and
- energy cluster in the calorimeters.

They are stored in Data Summary Tapes (DST). The DST data is then calibrated using the new calibration constants which were determined in each beam condition and stored to the CTL tapes named DSTPASS2.

4.2 Event reconstruction

4.2.1 Momentum measurement

The raw data was first corrected for any channel-to-channel variation of electronics. The spatial positions of "hits" in the TPC were then determined using pad signals, and particle tracks were searched among these points. Each found track was fitted to a helix, and the charge and momentum were assigned.

We define the coordinate system in the TOPAZ detector as shown in Fig. 4.2. The global coordinate in the TOPAZ detector is defined by x, y and z. The origin of the coordinates is the detector center. The ξ, η and ζ are coordinates fixed on the TPC sector. The ξ-axis is along the sense-wire direction, the η-axis points in the radial direction at the center line of the sector, and the ζ-axis is along the beam line. The details concerning this section can be found in reference [45].

Space-point reconstruction

The pad signal of each channel was first corrected for any electronics variation, and was then examined as a function of the CCD bucket number. Contiguous signals were grouped into a cluster to form a ζ hit. The peak pulse height and the ζ position of the cluster were calculated by fitting the highest three CCD buckets to a parabola. Clusters were then searched in the ξ direction. If signals in contiguous pads had roughly the same ζ positions (within 1cm), theses signals were combined into a cluster.

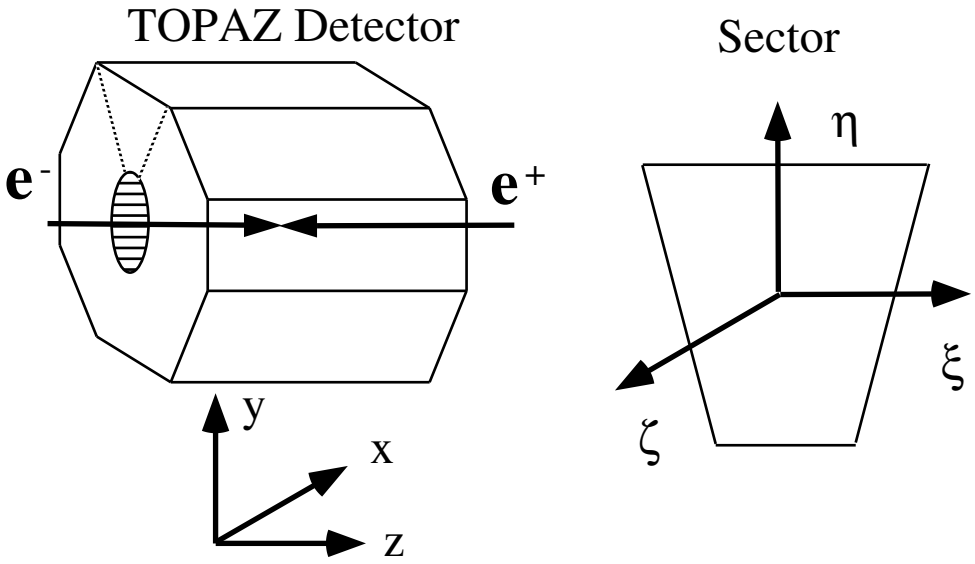

Figure 4.2: The definition of the coordinate system in the TOPAZ detector.

When a cluster was found, the ξ and η positions of the cluster were determined. Since the charge distribution along the pad row has approximately a Gaussian shape, the ξ position was calculated by fitting the highest 3 pad pulse heights to a Gaussian. If the cluster had only two pad signals, the pre-determined width of the Gaussian was used in the fit. The η position of the cluster was calculated by taking the centroid of the signals of five wires nearest to the pad row.

The position resolutions in ξ and ζ were studied using cosmic-ray tracks; typical values were obtained as $\sigma_\xi = 230\mu m$ and $\sigma_\zeta = 340\mu m$.

Track reconstruction

To find tracks from the reconstructed hits in the TPC, all found space points were first filled in a 2-dimensional histogram with ϕ and $z(R_{ref})$ axes such that

$$\begin{aligned} \phi &= tan^{-1}(x/\sqrt{x^2+y^2}) \\ z(R_{ref}) &= z \times (R_{ref}/R), \end{aligned}$$

where R_{ref} is the radial position of the fixed reference point. The space points associated to a track from the origin with a relatively high momentum were clusterized in a bin of the histogram. The track finding began by searching for a bin containing more space points than a given threshold. The threshold was set at 9 in the beginning, which corresponded to 10 pad raw hits; it was then lowered by

one when all of the bins above the current threshold were found. Lowering of the threshold was repeated until the threshold became two (three pad rows).

To test whether the space points in the bin formed a track or not, three space points which spanned the largest lever arm were chosen and checked as to whether they were on a single helix. If the space points were on a helix, other space points in the bin were checked as to whether they were consistent with the helix. If not, another set of three space points were chosen and the test was repeated. If a sufficient number of space points could be associated they were recognized to form a track and were fitted to a helix function.

Before the helix fitting, the space points were corrected for any dependence on the track angle to the sectors. The helix function was parametrized as follows:

$$\begin{aligned} x &= X_0 + d_\rho \cos\phi_0 + \frac{\alpha}{\kappa}(\cos\phi_0 - \cos(\phi+\phi_0)) \\ y &= Y_0 + d_\rho \sin\phi_0 + \frac{\alpha}{\kappa}(\sin\phi_0 - \sin(\phi+\phi_0)) \\ z &= Z_0 + d_z - (\frac{\alpha}{\kappa})\phi\tan\lambda \end{aligned}$$

where

$\vec{X_0}$	=	$\begin{pmatrix} X_0 \\ Y_0 \\ Z_0 \end{pmatrix}$	;	The position of the pivot.
$\vec{d}$	=	$\begin{pmatrix} d_\rho\cos\phi_0 \\ d_\rho\sin\phi_0 \\ d_z \end{pmatrix}$	;	The difference vector between the helix and the pivot at $\phi = 0$.
κ	=	$\frac{Q}{P_T} \rightarrow \rho = \frac{\alpha}{\kappa}$	;	The signed radius of the helix. Where P_T is the transverse momentum of the helix.
ϕ_0			;	The azimuthal angle of the pivot with respect to the center of the helix $+ \frac{\pi}{2}\cdot(Q/\lvert Q\rvert + 1)$.
$\tan\lambda$			;	The dip angle of the helix.
α	=	$\frac{1}{cH}$	;	A constant to convert curvature to momentum. Where c and H indicate the light velocity and the magnetic field strength, respectively.

These parameters are shown in Fig.4.3. The parameters to be determined by the fit are $(d_\rho, \phi_0, \kappa, d_z, \tan\lambda)$.

The fitting of the helix was achieved by minimizing χ^2 defined as

$$\chi^2 = \sum_i ((\frac{\xi_i - \xi(\eta_i)}{\sigma_{\eta_i}})^2 + (\frac{z_i - z(\eta_i)}{\sigma_{z_i}})^2),$$

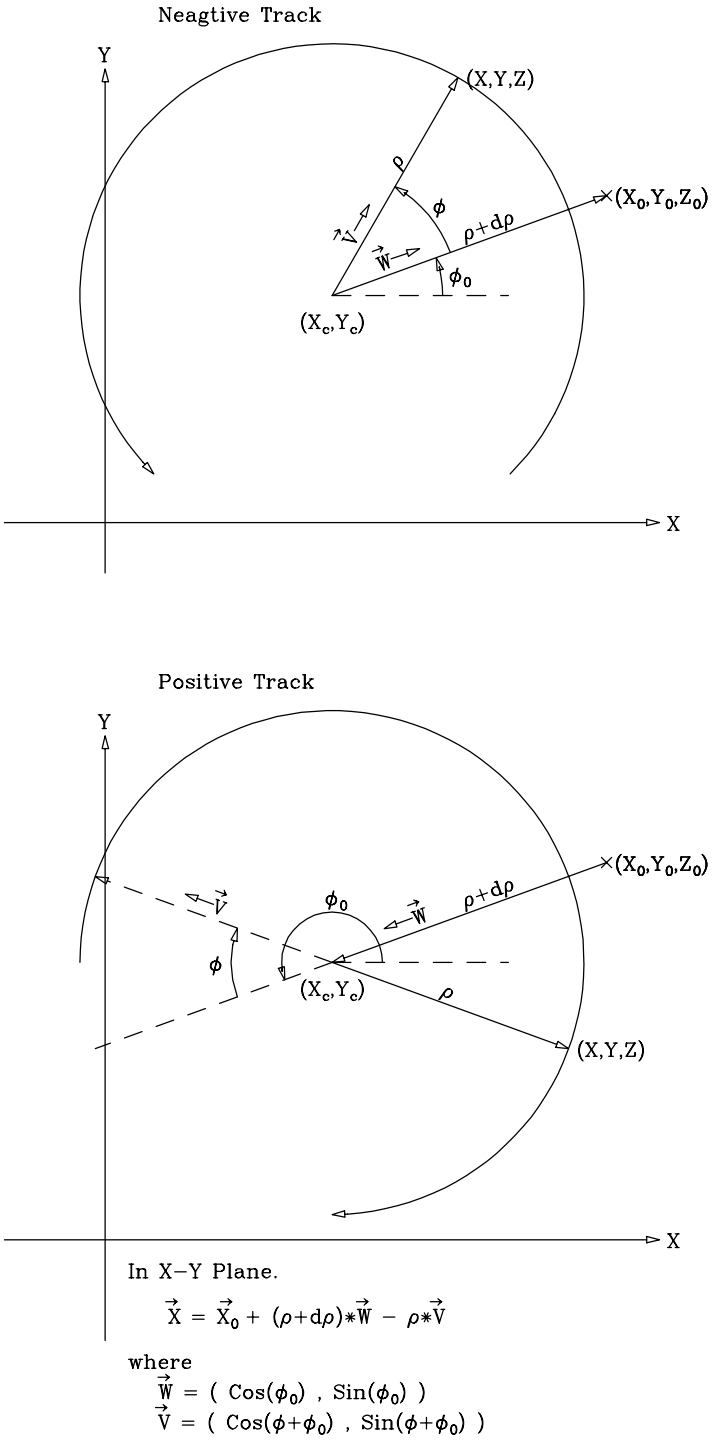

Figure 4.3: The helix parametrization of charged track in the TPC.

where ξ_i and z_i are the measured position in the i'th pad row and $\eta(\eta_i)$ and $z(\eta_i)$ are the expected position by the helix. We checked this χ^2 and made a final decision as to whether to recognize the space points as a track or not.

After all histogram bins forming tracks were found, the space points which were not recognized as tracks were then examined. From the remaining histogram bins, the bin containing the largest number of space points was searched for. The inner-most space point in the bin was chosen to be the origin (pivot) of the new histogram. The new histogram was defined with wider bins so that the space points of a low-momentum track could be clusterized in a bin as a new track candidate. The bins were tested in the same way as described above.

The performance of the track reconstruction was studied by using simulations. The tracking efficiency for hadronic events was 92.5% with no P_T cut and 94.2% with a P_T cut at 0.2 GeV/c. The efficiency plateau did not reach 100% because of sector boundaries and shallow tracks as well as nearby tracks giving overlapping pad hits.

Track Refinement

Although the gating grid prevents the feed-back of positive ions into the drift space and reduces the distortion in the electric field in the TPC, a small amount of distortion still remains, resulting in a systematic shift in the space-point determination. The dielectric material in the TPC, such as field cages, are also a source of distortion.

In addition to electrostatic distortion, the spatial positions of the TPC sectors may deviate from the designed position. This also causes a shift in the determination of the space points.

The electrostatic distortions in the $r\phi$ plane were parametrized as

$$\Delta x_\phi = a_0(r - r_{ref})^2,$$

where Δx_ϕ is the position displacement in ϕ due to the distortion. The deviations of the sector position in the $r\phi$ plane ($\Delta\zeta$, $\Delta\eta$) are parametrized as

$$\Delta\xi = d_\xi - \delta\eta$$

and

$$\Delta\eta = d_\eta + \delta\xi.$$

The shift in the z direction (dz) was expressed so as to include both the electrostatic distortion and the position displacements of the sectors, and was parametrized

as

$$\Delta z = d_z + d_v z.$$

These parameters were defined for each sector. The parameters of the electrostatic distortions were determined based on a comparison of two cosmic-ray data taken when the beam was on and off. The parameters of the position displacements of the sectors and the shift in the z-direction were determined based on a comparison of two measurements for a cosmic-ray track by two sectors when the beam was on. The space points calculated in the previous sections were corrected for any distortions using these parameters.

Finally, the space points were fitted to a helix again in order to assign the sign of the charge and momentum to the track. The momentum in the xy plane (P_T) and along the z-axis (P_L) were expressed using the helix parameters as

$$P_T = |\frac{Q}{\alpha\kappa}|$$

and

$$P_L = P_T tan\lambda,$$

where

$$\alpha = \frac{1}{cB} = 333.56\ cmGeV^{-1}.$$

Q is the charge of the particle, c the velocity of light, and B the strength of the magnetic field (1.0 tesla). The sign of the charge was determined from the sign of κ.

The resolution of the momentum measurement was estimated using the cosmic rays [46]. The resolution was studied by comparing two measurements in opposite sectors for a cosmic-ray track. The momentum resolution was studied as a function of momentum, and was obtained as

$$\frac{\Delta P_T}{P_T} = \sqrt{[(1.5 \pm 0.1)P_T]^2 + (1.6 \pm 0.3)^2}\%.$$

The effect of distortion corrections was studied using Bhabha events. Fig.4.4 shows the curvature distribution for e^+e^- tracks in the Bhabha events. The momentum resolution was measured to be $(1.7 \pm 0.1)P_T\%$.

4.2.2 dE/dx measurement

The energy loss per unit length (dE/dx) is a function of the velocity (β) and the charge (Q) of a particle. This information provides powerful tool for identification

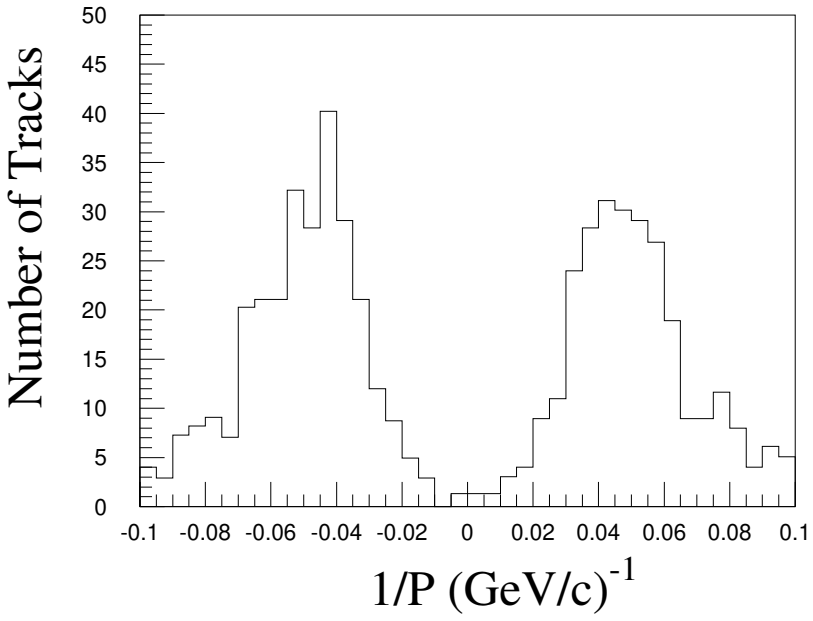

Figure 4.4: The curvature distribution for Bhabha events.

the kind of particles. Its performance is particularly crucial for the inclusive-electron analysis in this thesis. In this section we examine the property of the dE/dx curve and discuss what determines the dE/dx resolution. In practice, the dE/dx resolution suffers from various systematic shifts due to temperature, pressure, high voltage, electronics and so on. We need to improve the resolution as much as possible in order to maximize the searchable region.

Theoretical consideration

Average energy loss

When a charged particle traverses a medium, it interacts with atoms in the medium. The dominant process of energy loss is atomic excitation. The probability of exciting an atom scales as the square of the transverse component of the incident particle's electric field with respect to its velocity vector. The transition probability, and hence the energy loss, scales as the charge of the incident particle squared.

Qualitatively, the average energy loss ($< dE/dx >$) in the material can be described as a function of the velocity (β) and charge (Q) of the particle. The

function can be approximately written as (Bethe-Bloch equation):

$$< \frac{dE}{dx} > \approx \frac{4\pi n Q^2 e^2}{m_e e^2 \beta^2} (ln \frac{2 m_e \beta^2 \gamma^2}{I^2 + (\hbar\omega)^2 \beta^2 \gamma^2} - 2\beta^2),$$

where

I is the logarithmic mean atomic ionization potential,

ω is the plasma frequency of the medium,

n is the electron density of the medium,

m_e is the electron mass,

e is the electron charge, and

Q is the charge of the incident particle.

The values of $< dE/dx >$ fall as $1/\beta^2$ with increasing the momentum of the particles (non relativistic region). The fall off is due to the fact that a particle traversing the material spends less time in the electric field of atoms, and, hence, transfers less energy as the particle's velocity increases. The ionization becomes minimum at $\beta\gamma \simeq 3$, and then $< dE/dx >$ rises logarithmically as the momentum increases (relativistic region). This "relativistic rise" is the result of the relativistic increase in the transverse electric field of the incident particle. The $< dE/dx >$ finally reached the plateau due to the "density effect" caused by the polarization of the medium.

Energy-loss distribution

There are two contributions to the shape of the energy-loss distribution: atomic excitations and $\delta - ray$ production. The $\delta - ray$ contribution falls inversely proportional to the energy-transfer squared $(1/(\Delta E)^2)$, because this is the classical Rutherford scattering for free electrons. This process makes a long tail, called Landau tail, in the energy-loss distribution up to the kinematical limit. The peak of energy loss distribution is due to atomic excitation, which is the dominant energy-loss process. Argon, which is the main component of the TPC gas, has three shell structures: K, L, and M. The energy levels are 3.20 keV, 248 eV, and 16 - 52 eV, respectively. Since the collision probability with an electron is roughly proportional to its energy level, the lower energy-level excitations give a narrower dE/dx distribution.

dE/dx measurement

Derivation of the energy loss

The energy loss was measured using wire signals of the TPC. First, the wire signal clusters were searched in the z direction in the same way as the pad clusters. The pulse height of a cluster was determined from the peak amplitude of a parabola fitted to the highest 3 CCD buckets in the cluster. The z position of the cluster was also determined from the fit. The cluster was then associated to a track using the z information. If the cluster was within 1 cm of the track in the z direction, and not associated to other tracks, the cluster was linked.

The pulse-height amplitude was converted into the energy-loss value by two steps. The first was a correction for any non-linearity of the electronics. The second was a correction for the wire-to-wire gain variation. Details concerning the calibration are described in the following subsection.

Since a TPC sector has 175 sense wires, the energy loss for a track was sampled every 4-mm segment up to 175 independent data. A single variable, which is similar to the most probable energy loss, was deduced from the data sample. The final dE/dx was then derived by making various corrections, which are discussed later.

Calibrations

Prior to the experiment, after the electronics were calibrated by pulsing the shielding grid wires with various test-pulse amplitudes, the calibration curve for each channel was determined. The linearity of our electronics is better than 0.5% below the saturation point of CCD's. The remaining non-linearity, appreciable near to the saturation point, is corrected using this calibration curve.

After an electronics calibration, a correction for the wire-to-wire gain variation is made. Each sector is equipped with three rods having a ^{55}Fe X-ray source for each wire. Each rod can be moved pneumatically behind the hole on the cathode plane to irradiate wires. The wire-to-wire gain variation is corrected by calibrating the pulse height for the main peak of 5.9 keV for each wire. This calibration reduces the gain variation over a sector within a 3% level, and also gives the factor necessary to obtain the absolute value of the measured dE/dx.

The 65%-truncated mean

Fig. 4.5 shows the measured energy-loss distribution in the TPC for minimum ionizing pions. The shape is asymmetric and has the long tail at the higher side

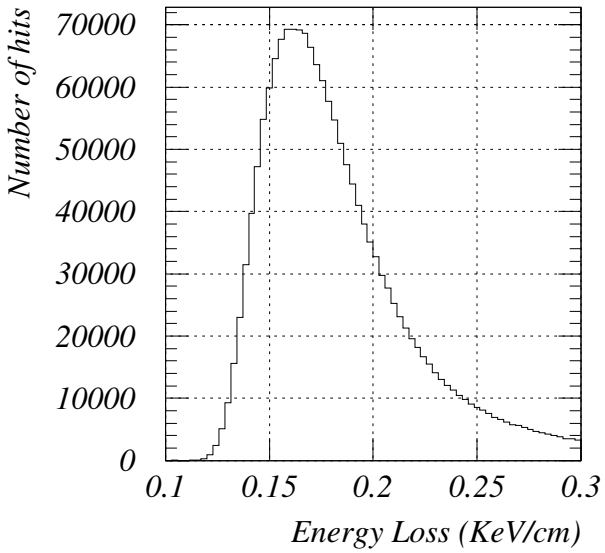

Figure 4.5: Pulse-height distribution obtained by the TPC wire signals for minimum ionizing pions.

(Landau tail). Therefore, a simple mean of the dE/dx sample for a track is not a good parameter for particle identification. The most probable energy loss or the mean value around the peak is a better parameter. We adapted the mean of the lowest 65% in the data sample (the 65%-truncated mean) as an estimator for the energy loss of a track. In the following we use dE/dx as in this meaning.

Corrections

To achieve a good resolution in dE/dx measurements, one must reduce the systematic shifts of the gain. In this section we discuss the systematic shifts of dE/dx and how we correct them.

In the TPC, measuring the energy loss is an indirect process. An implicit assumption is that the number of ionization electrons produced per track length is proportional to dE/dx of the charged particle. As electrons in the gas drift to the sectors they defuse; some fraction is absorbed by impurities, such as O_2, in the gas. Since the maximum drift length is more than 1 m, this effect is not negligible. We determined the attenuation factor using minimum ionizing pions in the momentum range between 0.5 and 0.6 GeV/c. Fig. 4.6 shows the measured

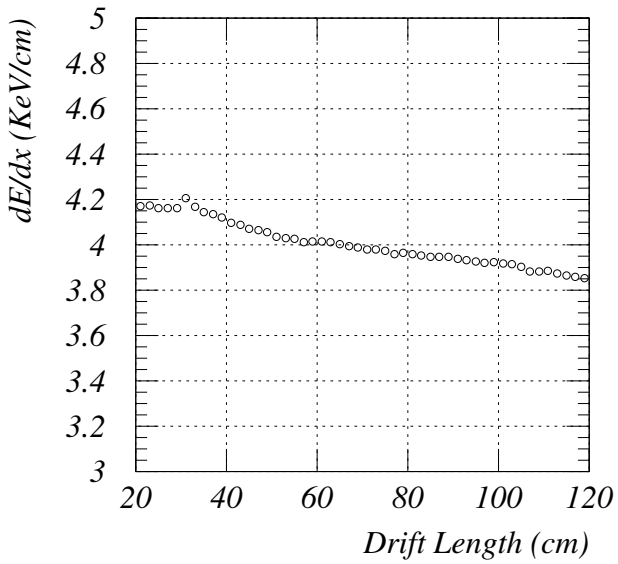

Figure 4.6: dE/dx as a function of the sample thickness in logarithm after a segment-length correction.

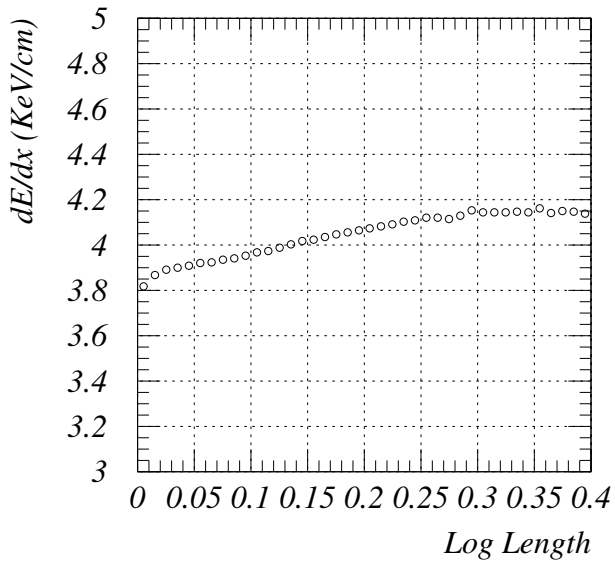

Figure 4.7: dE/dx as a function of the density from the nominal value.

value of dE/dx as a function of the drift length. We correct this effect using following function:

$$PH_{correct} = PH_{measured} \times (1 + C_1 L),$$

where

PH is the pulse height, and

L is the drift length.

The attenuation factor (C_1) is typically 7% per meter.

The gain shift due to the sample thickness dependence was also corrected using the minimum ionizing pions. Fig. 4.7 shows dE/dx vs. the path length on the logarithm scale. This systematics was corrected using

$$PH_{correct} = PH_{measured} \times (1 - C_2 \times log(X)),$$

where

X is the path length normalized by 4 mm.

The factor C_2 was determined to be 0.2.

The electric fields near to the sense wires also affect the avalanche process. The dependence of the pulse height on the high voltage was parametrized as

$$PH_{correct} = PH_{measured} \times (1 - C_3 \times \frac{\delta V}{V_0}),$$

where

V_0 is the nominal high voltage (1970V) on the sense wire, and

δV is the variation of the voltage.

The correction factor (C_3) of the pulse height was determined using data taken in low high-voltage cosmic-ray runs. A 1% high-voltage change corresponds to a 17% change in the gain.

The electrons approaching the sense wires pass through the avalanche process. As the gas density increases the mean-free path of electrons becomes shorter and the soft collisions in which the electrons do not ionize the atoms increase; hence, the amplification factor drops. The gas density is proportional to the pressure and inversely proportional to the temperature. The pressure was well controlled, and its variation was less than 0.04% throughout this experiment. The temperature of the gas was increased by about 2°C during the summer. Fig. 4.8 shows dE/dx vs. the variation in the gas density. From the temperature change, we found that

$$PH_{correct} = PH_{measured} \times (1 + C_4 \times \frac{\delta \rho}{\rho_0}),$$

where

ρ_0 is the nominal gas density, and

$\delta \rho$ is the variation of the gas density.

The C_4 value was 6.0. A 1°C temperature change corresponds to about a 2% change in the gain.

After these corrections, we again carried out a wire-to-wire gain calibration. The event sample with minimum ionization pions were used for this purpose. After the pulse-height distributions for each wire were made and the correction factors were derived, a run-dependent correction was carried out. There were still unknown factors which changed the energy-loss values. Each step used a single run corresponding to a few 1000 beam events.

Finally, we derived the dE/dx distribution for momentum between 0.5 and 0.6 GeV, which was the minimum ionizing pion region. There were two peaks

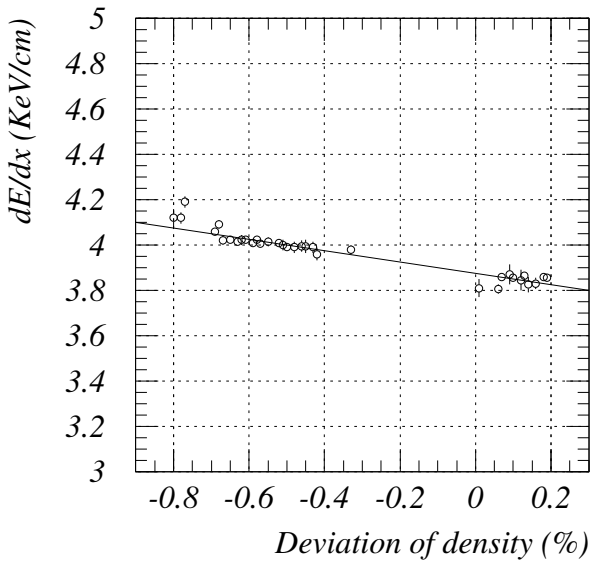

Figure 4.8: dE/dx vs. momentum for tracks in more-than-one-track events.

corresponding to pions and electrons. For several reasons, the relationship between these two peak values changed nonlinearly. One reason was an over-value setting of the threshold values in the electronics during some experiments. The other was a selection bias in the event pre-selection code in order to reduce the data size, mainly due to the vacuum condition. These caused a nonlinear offset in the pion dE/dx value. We thus corrected these by normalizing them to the initial experimental values in which the threshold values were considered to be sufficiently low. Furthermore, we fitted the width of two dE/dx peaks using the common ratio to the center values of the peaks using two Gaussians. The fitted width was considered to be the error of the dE/dx determination; the χ^2s calculation is described later.

Velocity dependence of dE/dx

The dE/dx curve as a function of the particle velocity was determined from the data. Although theoretical calculations of the dE/dx curve reproduce the data fairly well, they are not adequate for particle-identification purposes, especially in the relativistic rise region. The data used for the determination were those from protons for the small-β region, cosmic-ray muons and minimum ionizing pions

coefficient	value
c_0	6.2133
c_1	2.1340
c_2	-1.6116
c_3	-0.19783
c_4	0.0363802
c_5	-0.35785
c_6	1.4957
c_7	-0.16234
c_8	-0.95077
c_9	0.379

Table 4.1: Coeficients of the 9'th-order polynomial function.

for low $\beta\gamma$, and electrons for the relativistic rise region. The data are fitted to a ninth-order polynomial parametrized as

$$\frac{dE}{dx} = \frac{1+(\beta\gamma)^2}{(\beta\gamma)^2}\sum_{i=0}^{9} c_i(\frac{ln(\beta\gamma)-4}{5})^i - 0.70659,$$

where the c_i are given in Table 4.1. Fig. 4.9 shows the dE/dx vs. momentum for tracks in more-than-three-track events. The bands of electrons, pions, kaons and protons can be clearly seen.

dE/dx resolution

The resolution of dE/dx was studied using the minimum ionizing pions. Fig. 4.10 shows the dE/dx distribution of pions with momenta between 0.5 and 0.6 GeV/c. The resolution was estimated by fitting a Gaussian function to the distribution, and was obtained as $\sigma_{dE/dx} = 4.6\%$. The resolution for Bhabha events was also measured as $\sigma_{dE/dx} = 4.4\%$.

4.2.3 Energy measurement

Electrons and photons make electromagnetic showers in the calorimeters, and deposit energies in several counters. We must reconstruct energy clusters from the energy deposits.

The raw data from the BCL consists of digitized pulse heights for lead glass counters. These digitized data are converted into energy deposits counter by

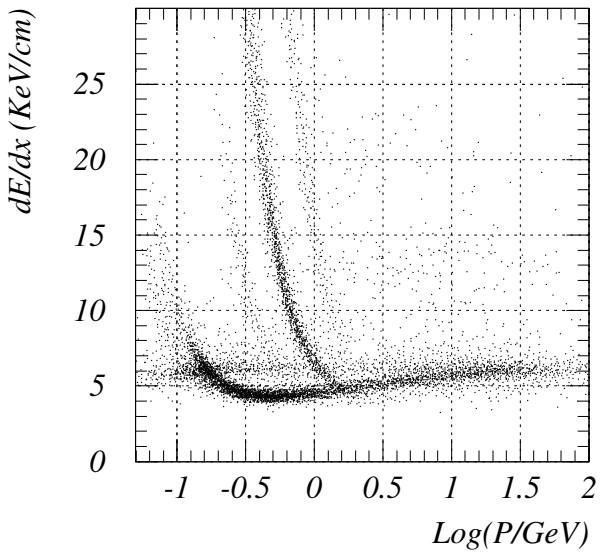

Figure 4.9: dE/dx vs. momentum for tracks in more-than-one-track events.

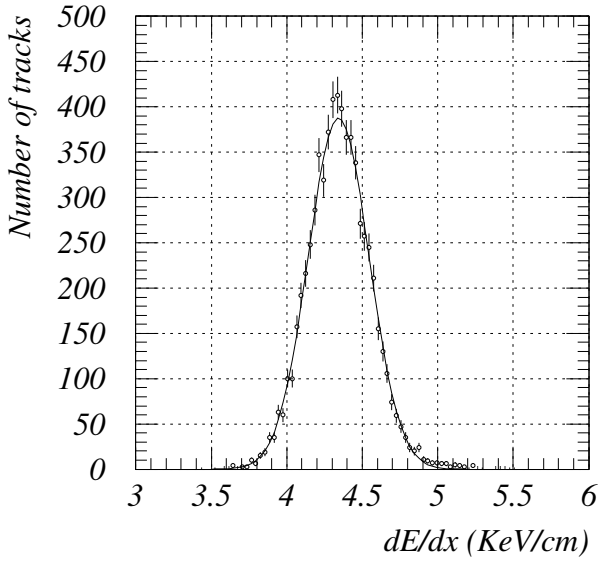

Figure 4.10: dE/dx distribution for minimum ionizing pions.

counter bases. The energies and positions of the clusters produced by electrons and photons hitting the calorimeters are reconstructed as follows:

1. We searched the counter B_1 which have the largest deposit energy of E_1;

2. If the counter B_2 neighboring to B_1 had the deposit energy of E_2, it was added as the same cluster including B_1;

3. If the counter B_3 neighboring to B_2 with the deposit energy of E_3 satisfied the conditions:

$$E_2 > C_1 E_1$$

or

$$E_3 > C_2 E_1 \quad \text{and} \quad E_3 < C_3 E_2,$$

B_3 was considered to belong to the same cluster. Here C_1, C_2, and C_3 are constants optimized so that electrons and photons to be well reconstructed. Using Monte-Carlo simulation, the constants were decided to be 0.65, 0.08, and 1.20 for C_1, C_2, and C_3, respectively.

The procedure was repeated for all counters with energy of greater than 45 MeV.

The average cluster position in zϕ-plane was determined by the energy-weighted mean of the counter positions:

$$X = \frac{\sum_i X_i \cdot E_i^p}{\sum_i E_i^p}$$

where X_i denotes the z or ϕ coordinate of i-th lead glass counter defined at the front face, and E_i is the energy deposited in the i-th counter. The parameter p was optimized to be 0.26 and 0.34 for z and ϕ, respectively, by the EGS4 simulation[47]. The R coordinate of the cluster was determined at the depth of the shower maximum with assuming the cluster to be a photon which coming from the interaction point.

4.2.4 Re-clustering for BCL cluster

There expected that many daughter clusters be produced from energetic electromagnetic particles. In order to reconstruct the energy and position more exactly, we therefore carried out the re-clustering for BCL clusters. The method for electromagnetic energy clustering is described as follows:

1. We searched the maximum energy counter among 8 neighboring counters (at the +z or -z edge of the BCL, 5 counters) for counter by counter;

2. If the neighboring maximum counter energy was higher than its energy, the counter was merged to the neighboring one;

3. After the above procedures were iterated, the clusters were formed;

4. The cluster energy was calculated by summing the total counter energy in the cluster;

5. The azimuth angle (ϕ) and the z-position were calculated using the energy-weighted mean of the counter positions *i.e.*,

$$X = \frac{\sum_i X_i E_i}{\sum_i E_i};$$

6. The depth of the cluster center was calculated according to $X = ln(E/E_c) + 1.5$ (radiation length), where E is the cluster energy and E_c (12.6 MeV) is the critical energy of the BCL (lead glass);

7. The radial position (R) of the cluster was calculated according to the formula $R = R_{BCL} + X_0 \cdot X \cos\theta$, where R_{BCL} and X_0 are the inner radius and the unit radiation length of the BCL, i.e. 176cm and 1.7cm, respectively. Here, θ was assumed to be that of the maximum energy counter in the cluster, at first;

8. From z and this R, the θ was re-calculated; and

9. R and θ calculations were iterated two times.

4.2.5 Energy calibration

The monitoring system for the gains of 4300 counters comprises just one light source and an optical-fiber system. As the light source, a xenon flash lamp having a 3mm gap was chosen, because the emission spectrum resembles Čerenkov light. The amount of light received at a counter corresponds to about 7 GeV in energy. In order to correct for any variation in the light intensity of the xenon flash lamp, reference counters were placed in a temperature-controlled box. At each reference counter a NaI(Tl)-^{241}Am light pulser was attached to measure the gain independently. The gain variation can be corrected to the 0.5% level.

The gain of each counter was calibrated with 4, 2, and 1 GeV electron beams from the IT1 beam line [48] at the 8-GeV Accumulator Ring (AR) at KEK.

We have accumulated Bhabha scattering events, after standard cuts of requiring two clusters of deposited energy greater than 1/3 of the beam energy at $|\cos\theta| < 0.77$ satisfying an acolinearity angle being less than 10^o. The obtained resolution was 4.5%, apparently dominated by the non-uniformity in the gains of individual counters. The angular resolution was obtained to be 0.36^o. Calibration of the individual counters was carried out using these Bhabha events. However, not all of the counters have been calibrated yet, due to a lack of statistics.

The electron energy-loss in the material in front of the BCL was investigated by studying the E/P for electrons. In this study we used an experimental two-track sample selected by the following criteria, expecting these to be dominantly $e^+e^- \to e^+e^-e^+e^-$ events:

1. The number of charged tracks with $P_T > 0.15$ GeV, the polar angle $|\cos\theta| < 0.83$, and the number of degrees of freedom (N.D.F.) of charged-track fitting ≥ 3 had to be 2;

2. The number of the BCL clusters with $E_{cluster} > 100$ MeV had to be at least 1; and

3. The visible energy (E_{vis}) of the event had to satisfy $E_{vis} < 30$ GeV, where both the charged tracks in the TPC and the clusters in the BCL were used.

Most of the selected events were expected to be two-photon events of $(e^+e^-)e^+e^-$, $(e^+e^-)\mu^+\mu^-$, and $(e^+e^-)\pi^+\pi^-$. The remaining ones were $\mu^+\mu^-$, $\tau^+\tau^-$, $e^+e^-\gamma$, etc. The used data corresponded to an integrated luminosity of 24.5 pb^{-1} at $\sqrt{s} = 50 \sim 60.8$ GeV. These selection cuts left 9120 two-track events.

To separate electron tracks from muons and pions, we used energy-loss (dE/dx) information from the TPC and TOF as follows: (1) The electron-candidate tracks were required to have dE/dx in the range of $5.5 \leq$ dE/dx ≤ 7.5 keV/cm; (2) the confidence level (CL) for the electron hypothesis by the TOF information had to be > 0.01. We then calculated the E/P ratio of the energy measured by the BCL and the momentum measured by the TPC. The TPC-BCL combination was chosen when the distance between the BCL cluster and the extrapolated track was shortest. We only calculated the E/P for the TPC-BCL combination whose distance was less than 10cm.

To determine the BCL energy correction we fitted the E/P distribution with a second-order polynomial of the BCL energy. We used electron candidates which

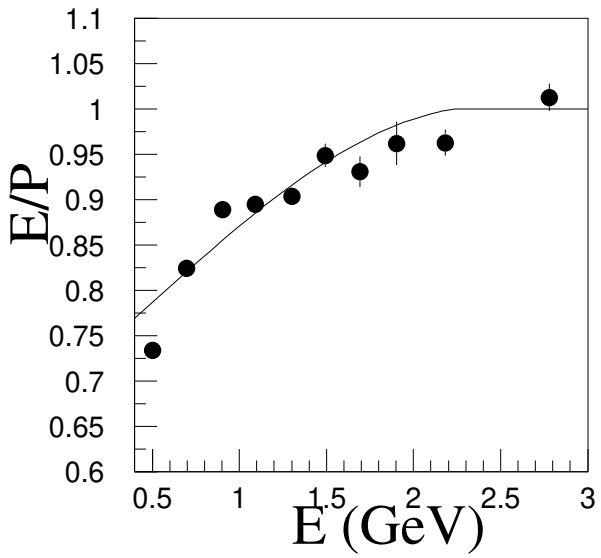

Figure 4.11: E/P ratio as a function of the BCL energy (filled circle). The solid line was obtained from a polynomial fitting (described in the text).

were in the energy range E < 4.0 GeV and the polar angle range $|\cos\theta| \leq 0.77$. The E/P-versus-energy distribution with the fitting curve is shown in Fig.4.11. Since real electrons should concentrate on E/P = 1, we obtained the following expression from the fitting result:

$$\begin{aligned} \frac{\Delta E}{E} &= 0.430 - 0.354 \cdot E + 0.072 \cdot E^2 \quad for \;\; E \leq 2.3 GeV, \; and \\ &= 0 \quad for \;\; E > 2.3 GeV. \end{aligned}$$

The E/P distributions in the momentum range $0.4 \leq P \leq 4.0$ GeV, E/P and momentum scatter plots with and without the BCL correction are shown in Fig. 4.12.

4.3 Luminosity measurement

The luminosity (L) is an important parameter for the e^+e^- collider experiments, which indicates the collision rate of beams. The observed number of events ($N_{measured}$) is given by;

$$N_{measured} = \varepsilon \cdot \sigma \cdot \int_{\delta t} dt$$

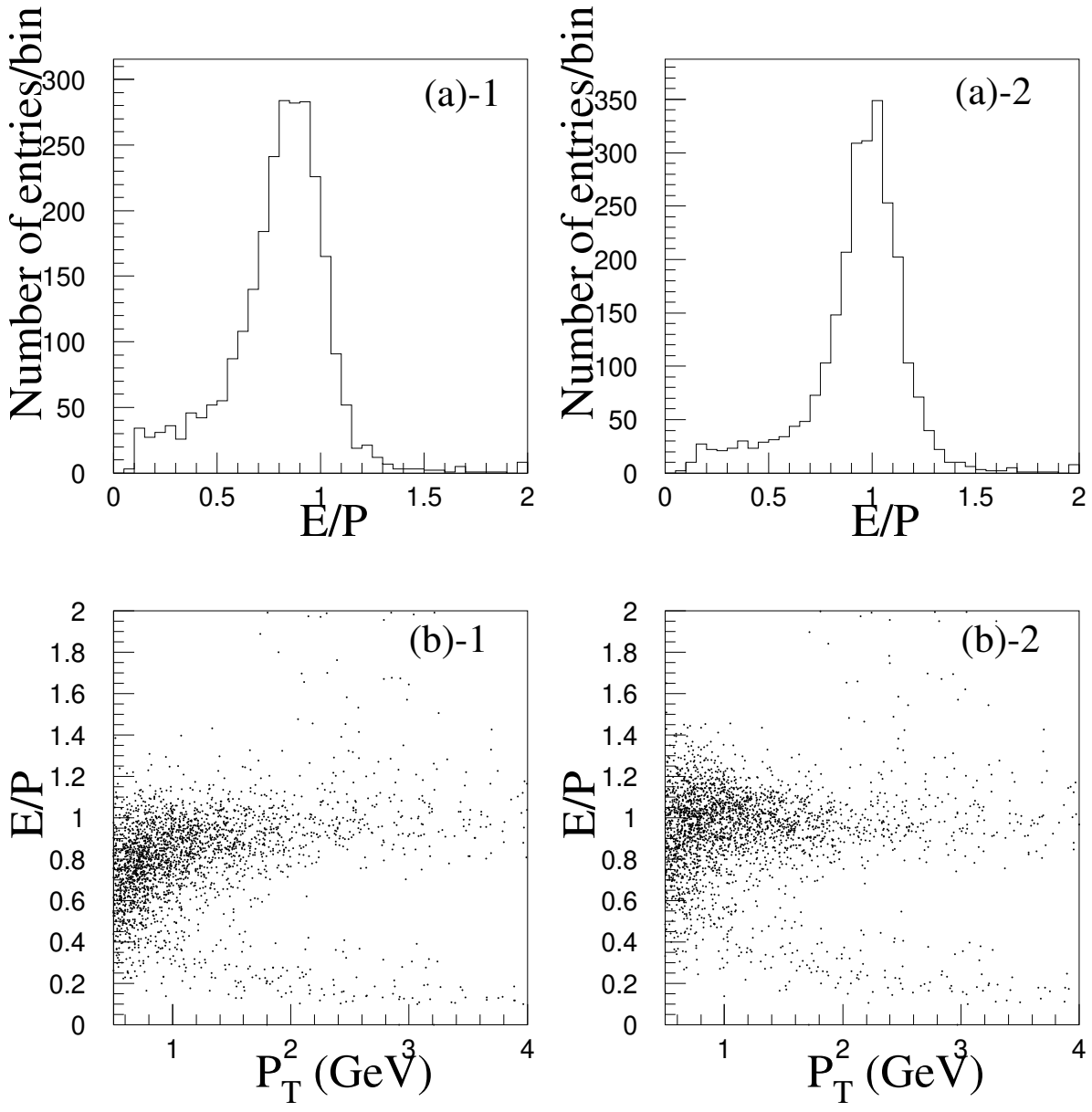

Figure 4.12: E/P distributions in the momentum range $0.4 \leq P \leq 4.0$ GeV [(a)-1 and 2] and scatter plots of E/P vs. energy [(b)-1 and 2]. Indices 1 and 2 denote that without and with the BCL correction, respectively. The equation of the correction function is given in the text.

where ε, σ, and $\int_d t$ are the detection efficiency, the cross section, the integrated luminosity which is the luminosity integrated over the time during the experiment (Δt), respectively. In the e^+e^- collider experiments, the integrated luminosity is obtained using small angle Bhabha events ($e^+e^- \rightarrow e^+e^-$), since the cross section for the process is well described in the framework of QED, the high statistics are expected, and it is relatively easy to detect the elastically scattered electrons.

The integrated luminosity used in this analysis was determined from Bhabha scattering events observed in the ECL. The main selection criteria are:

1. There must be one or more clusters having an energy greater than one third of the beam energy in the angular region of $0.866 <| \cos\theta |< 0.976$.

2. one cluster in +z hemisphere must be well contained, *i.e.* in the angular region of $0.895 < \cos\theta < 0.959$ to define acceptance clearly.

3. The acolinearity angle must be less than 10°.

The main background was the reaction $e^+e^- \rightarrow \gamma\gamma$, and was estimated to be 1.6%, for which the differential cross section was corrected. Other backgrounds such as τ pair production were found to be less than 0.3%. The systematic uncertainty of the luminosity measurement was estimated to be 4.0%, regardless of the beam energy, by comparing the luminosity values obtained in the different azimuthal regions of the ECL. As a cross-check, we also calculated the integrated luminosities using the BCL and the FCL, and the results agreed with that using the ECL within statistical errors throughout the experiment.

Chapter 5

Monte-Carlo simulation

In order to compare the experimental data with the theoretical predictions, a Monte-Calro simulation plays an important role. With the Monte-Calro method, we can generate the events according to the cross-section formula, estimate the detection efficiencies, and study the physical background contributions.

Fig.5.1 shows an analysis flow comparing the experimental data and the Monte-Carlo data based on the theoretical predictions. In this analysis, we carried out the Monte-Carlo simulation by several steps. At first, according to the theoretical cross-section formula, we carried out the event generation. Secondly, the generated events passed through the TOPAZ detector simulation so as to estimate the detection efficiency. The outputs have the same format as those of the real data. At the third step, we also carried out the trigger simulation in order to estimate the trigger efficiency.

As shown in the Fig.5.1, the Monte-Calro data was analyzed with the same selection programs as used for the real data. We then compare the real data and the Monte-Carlo data at observed level, and converted the number of the observed events to the cross section by taking account for the detection efficiencies obtained by the detector simulation.

5.1 Event generation

5.1.1 Parton generation

We used the BASES and SPRING program packages[49] for event generation at parton level. In the BASES program, the differential cross section is integrated over the regions which were allowed kinematically, and probability distribution (generating function) is produced. For this analysis, we use the cross-section

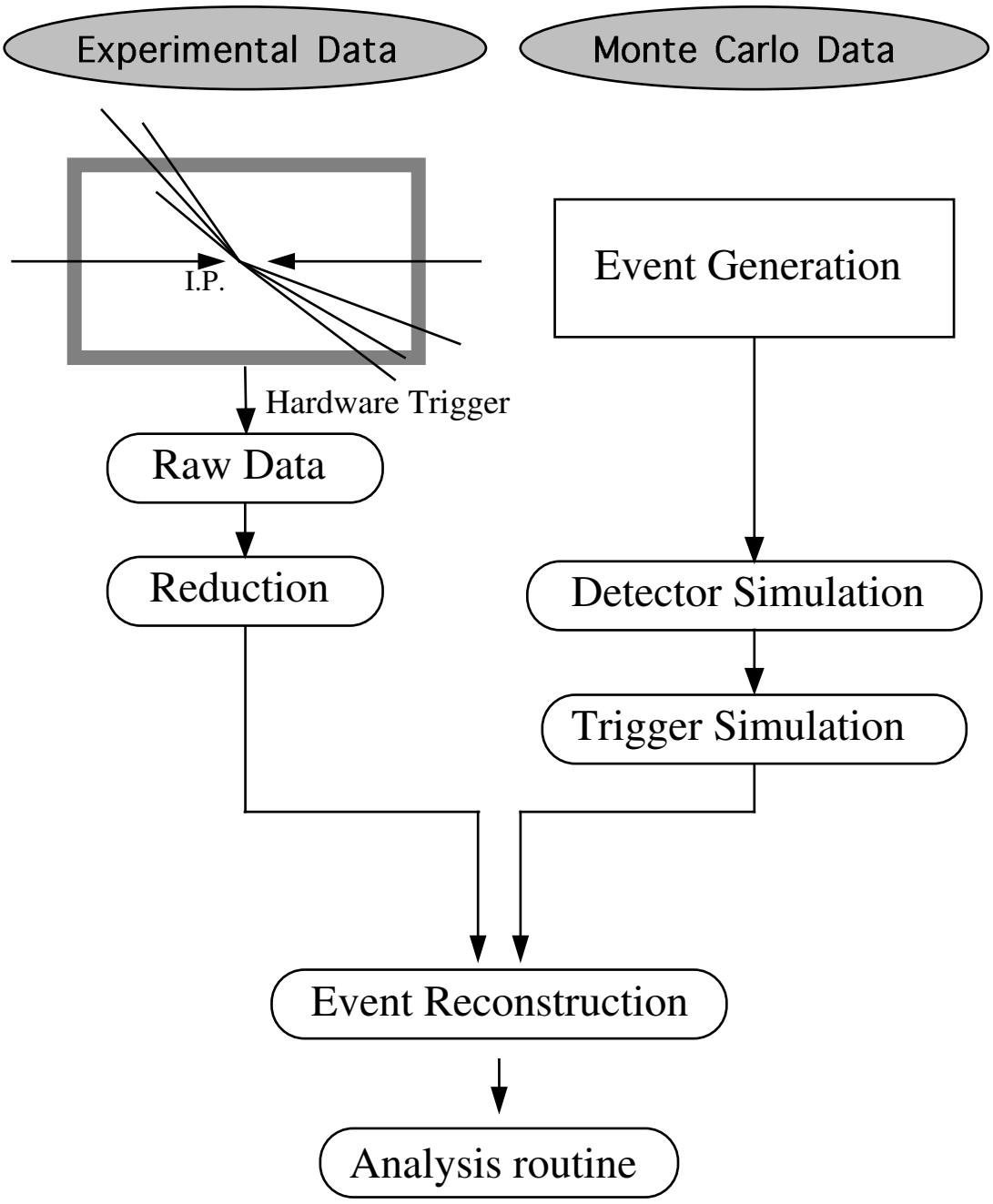

Figure 5.1: An analysis flow of the comparison of the experimental data and Monte-Carlo data.

formula expressed in Chapter 2. By SPRING, four momentum vectors of events are generated according to the probability distribution made by BASES.

In this analysis, the current charm-quark mass(m_c) used in the cross-section calculations was changed in the range 1.3 - 1.5 GeV in order to see the effect of the mass. The threshold was set at $2 \times m_{D^*} = 3.74$ GeV (m_{D^*}: D^* meson mass) for the mass of the $\gamma\gamma$ system and at 2×1.6 GeV for that of the $c\bar{c}$ system.

In the resolved process, the remnant jets were generated in the beam direction.

5.1.2 Hadronization

The produced partons were then fragmented into hadrons (hadronization) by JETSET 6.3[50] program. In this analysis, we used the string fragmentation model without parton-shower option.

To describe the properties of the fragmentation, we used the fragmentation function: $f(z)$, which represent the probability that the hadron is found in the debris of a parton carrying a fraction z of its momentum. For charm-quark fragmentations, we used Peterson function,

$$f(z) \sim 1/z\{1 - \frac{1}{z} - \frac{\epsilon}{1-z}\}^2,$$

where we set the parameter ϵ to be 0.07. For light quarks, we used the symmetric function given as,

$$f(z) \sim \frac{1}{z}(1-z)^a \exp(-\frac{bm_T^2}{z}),$$

where m_T is the transverse mass of the hadron. The used parameters were default values of a=0.1 and b=0.7 GeV^{-2}. Transverse momentum of the hadrons is described by the Gaussian function of

$$f(P_T) \sim \exp(-\frac{P_T^2}{2\sigma_q^2}),$$

and we set $\sigma_q = 0.4GeV$.

In the JETSET, the constituent charm-quark mass($m_{const.}$) was set to be 1.6 GeV. To ensure energy conservation, we adjusted the momentum of the charm quark in the fragmentation stage as $P^2_{JETSET} = P^2_{gen} + m_c^2 - m^2_{const.}$.

5.2 Detector simulation

The generated events were passed through the TOPAZ detector simulator so as to take into account any acceptance and resolution effects.

This detector simulation was designed to take into account all conceivable interactions which the particles might experience in the detector, and to mimic the detector response to them as closely as possible. The structures and materials of the detectors are precisely coded in the program and each particle is propagated by a small step from the interaction point. At each step, such interactions as decays, multiple scattering, and bremsstrahlung take place according to the probabilities associated with them.

In the TPC region the averaged energy loss in the gas is calculated according to a formula determined from the minimum ionizing pions in real data, knowing the velocity and charge of the particle. The Landau fluctuation is taken into account by smearing the energy loss so as to be consistent with the experimental distribution. The smeared energy loss is translated to a pulse height on the corresponding wire to be sampled in order to mimic the digitized outputs. Because the time profile of the wire signal was experimentally found to be independent of the track angle, a single pulse-height shape function is used to calculate the pulse height in each time bucket. The pulse height is digitized if it is above the threshold, and is recorded as wire data. Pad signals are generated using the pulse heights of the relevant five wires near to the pad rows. The avalanches on the five wires induced a charge along the pad row. We assume that the induced charge is a Gaussian distribution, and is proportional to the corresponding wire pulse heights. The width of the Gaussian and the weight factors for the five wires are determined experimentally [51].

To simulate the electromagnetic shower development in the material, the EGS code is widely used [52]. The cut-off energy in the EGS program, when it is used, must be set at a value sufficiently lower than a critical energy for an accurate simulation, which consequently needs more CPU time. In the BCL, the electromagnetic shower is simulated by using the Bootstrap method to save CPU time [53]. This method utilizes pre-generated showers to obtain the shower density in cells of suitable size in the calorimeter. The development of a shower with an energy lower than the cut-off is replaced by them. Thus, once many sets of the frozen showers are prepared for various energies, the shower simulation can be carried out as accurately as that of the EGS code, while at the same time considerably reducing the CPU time.

For a nuclear interaction GEISHA 7 is used [54]. Short-lived particles such as K_s, π^0, and Λ are decayed in the simulator program while keeping secondary vertex information.

$\sqrt{s}$ (GeV)	Integrated Luminosity (pb^{-1})	Track trigger condition			
		pre-trigger		TPC trigger	Software trigger
		TCH-TOF	Back to Back		
58.0	1.64 ± 0.03 ± 0.07	1/32-3/32	1/16-3/16	1/8-5/8	
58.0	0.39 ± 0.01 ± 0.02	1/32-3/32	1/16-7/16		
58.0	2.02 ± 0.03 ± 0.08	1/32-3/32	1/16-3/16		
58.0	0.34 ± 0.01 ± 0.01				
58.0	4.61 ± 0.05 ± 0.18				
58.0	12.55 ± 0.08 ± 0.50				
58.0	8.81 ± 0.06 ± 0.35	1/32-7/32	1/16-9/16		
58.0	20.29 ± 0.10 ± 0.81				
58.0	3.84 ± 0.04 ± 0.15				on
58.0	34.82 ± 0.13 ± 1.39	1/32-7/32	1/16-5/16	1/8-3/8	
58.0	6.03 ± 0.05 ± 0.24				

Table 5.1: Trigger condition.

5.3 Trigger simulation

As described in the section3.3, the track trigger was designed to accept the low multiplicity events with little calorimeter energy deposit. Except for the tagged data which has large energy deposit by tagged beam electron, almost two-photon events ($\sim 90\%$) were accepted with the track trigger. In Table5.1, the track trigger conditions for used data are summarized. The condition was changed according to the beam condition.

The track pre-trigger which composed the track trigger determined the minimum acceptable P_T of a track. Since P_T of charged tracks in the two-photon events were generally low, the track pre-trigger was especially important. In order to estimate the track pre-trigger efficiency, we carried out trigger simulation at the same condition as the experimental data.

The P_T minimum threshold of the track pre-trigger was determined by the combination of the TCH and TOF signals. Using the cosmic ray events, the trigger efficiency as function of P_T was studied. The results are shown in Fig.5.2 with the closed circles. The charged tracks with $P_T > 0.3$, 0.7, and 1.0 GeV/c at 1/32:7/32, 1/32:5/32, and 1/32:3/32 TCH-TOF conditions were triggered, respectively. The solid lines in the figure indicate the trigger efficiencies estimated by the trigger simulations. Both results from the trigger simulations and the cosmic ray events agree within the error bars.

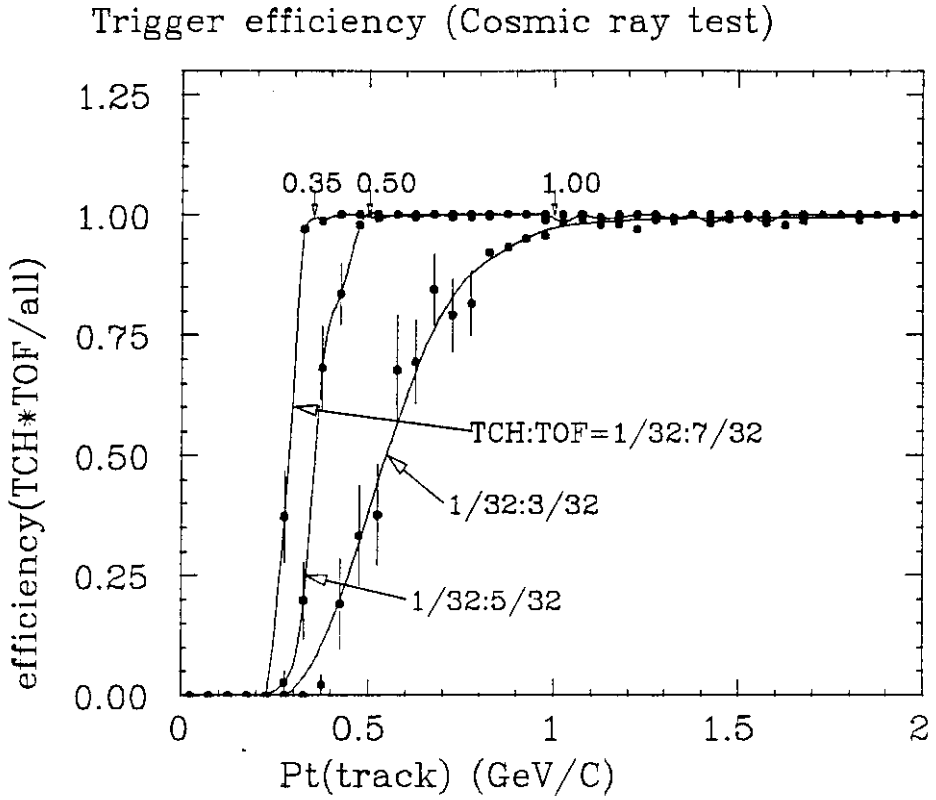

Figure 5.2: The trigger efficiency.